TU Delft

Delft University of Technology

Document Version
Final published version

Licence
CC BY

Citation (APA)
Su, H., Tang, K., van Beek, M., Rem, P., Bo, Z., Bheemireddy, R., Ali, N., Wu, Y., & Di Maio, F. (2026). Operating-window identification for magnetic density separation. *Results in Engineering*, *32*, Article 113344. https://doi.org/10.1016/j.rineng.2026.113344

Important note
To cite this publication, please use the final published version (if applicable).
Please check the document version above.

Copyright
In case the licence states “Dutch Copyright Act (Article 25fa)”, this publication was made available Green Open Access via the TU Delft Institutional Repository pursuant to Dutch Copyright Act (Article 25fa, the Taverne amendment). This provision does not affect copyright ownership.
Unless copyright is transferred by contract or statute, it remains with the copyright holder.

Sharing and reuse
Other than for strictly personal use, it is not permitted to download, forward or distribute the text or part of it, without the consent of the author(s) and/or copyright holder(s), unless the work is under an open content license such as Creative Commons.

Takedown policy
Please contact us and provide details if you believe this document breaches copyrights.
We will remove access to the work immediately and investigate your claim.

*This work is downloaded from Delft University of Technology.*

Results in Engineering 32 (2026) 113344

Contents lists available at ScienceDirect

Results in Engineering

journal homepage: www.sciencedirect.com/journal/results-in-engineering

Research paper

# Operating-window identification for magnetic density separation

Hongli Su [a,*], Kunning Tang [b], Max van Beek [a], Peter Rem [a], Zhenkai Bo [c], Rajeev Bheemireddy [a], Nishab Ali [a], Yongli Wu [a,*], Francesco Di Maio [a,*]

[a] Resource & Recycling, Department of Engineering Structures, Faculty of Civil Engineering and Geosciences, Delft University of Technology, Delft, 2628CN, the Netherlands

[b] School of Minerals and Energy Resources Engineering, The University of New South Wales, Sydney, NSW, 2052, Australia

[c] Institute of GeoEnergy Engineering, Heriot-Watt University, Edinburgh, UK

ARTICLE INFO

*Keywords:*
Magnetic density separation
Operating window
Feasible domain
Quasi-static density matching
Sensitivity analysis

ABSTRACT

Magnetic density separation (MDS) can separate millimetre-sized non-ferromagnetic particles, although suitable combinations of magnet inclination ($\theta$) and magnetic-liquid magnetization ($M_f$) depend on the separator geometry. We developed an operating map from a calibrated quasi-static density-matching model. Five measurements of magnetic-liquid density were interpolated piecewise linearly and combined with an exponential field-decay expression to calculate three bottom density-matching positions. Feasible conditions had to satisfy position ordering, tank and magnetic-field coverage, a 3.0 cm feed-zone boundary, and a minimum middle-product collection width of 0.45 cm. For $\theta = 12°$ and $M_f = 5300$ A/m, the calculated $x_h$, $x_l$, and $W_m$ were 21.920, 27.577, and 5.656 cm, respectively. The tested input perturbations and grid refinements produced only small changes in the reported metrics. Three independent separation runs, with triplicate ICP measurements for each sample, demonstrated density-based product partitioning at the selected condition. Broader validation will require testing additional operating conditions.

## 1. Introduction

Magnetic density separation (MDS) is a density-based technique for separating non-ferromagnetic particles in recycling, mineral processing, and resource-recovery applications [1–7]. Its ability to process millimetre-sized particles offers potential for coarse-particle pre-concentration before downstream processing [8–10]. Because comminution is highly energy intensive, rejecting low-value material before fine grinding may reduce the mass directed to the grinding circuit and, consequently, its associated energy demand [11–13]. In MDS, a non-uniform magnetic field generates a spatially varying effective density within a magnetic liquid (Fig. 1) [14,15]. Particles introduced into this field experience gravitational, hydrostatic-buoyancy, and magnetic-buoyancy forces and, under quasi-static conditions, are expected to approach regions where their density matches the local effective liquid density [14,15]. In the present inclined-magnet configuration, these density-matching regions correspond to different horizontal collection positions [14]. The present work focuses on operating-window identification and does not quantify grinding-energy reduction or total process-energy consumption.

The principal-controlled variables in this separator are the magnetic-liquid magnetization ($M_f$) and the magnet inclination angle ($\theta$). Magnetization sets the attainable effective-density range, while inclination changes how that field intersects the tank and collection system [15–18]. Their coupled effects determine the density-matching positions of the target particle classes and the spacing available for product collection. However, not every combination of $\theta$ and $M_f$ is practically usable. Under weak magnetic conditions, one or more target density-matching positions may lie outside the usable tank region. Other combinations may move a predicted cut beyond the tank boundary or reduce the middle-product collection width below that required by the particle size and splitter geometry. Selecting an operating condition therefore requires combinations of $\theta$ and $M_f$ that satisfy both the density-matching relations and the collection geometry of the separator (Fig. 1).

Coupled operating variables in mineral-separation processes have been investigated using factorial designs, response-surface methodology, constrained optimization, and multi-objective optimization [19–21]. Factorial and response-surface methods quantify interactions among operating variables and provide interpolated response surfaces

* Corresponding authors.
*E-mail addresses:* H.Su-3@tudelft.nl (H. Su), Y.Wu-7@tudelft.nl (Y. Wu), F.DiMaio@tudelft.nl (F. Di Maio).

https://doi.org/10.1016/j.rineng.2026.113344
Received 5 May 2026; Received in revised form 5 September 2026; Accepted 2 October 2026
Available online 3 October 2026
2590-1230/© 2026 The Authors. Published by Elsevier B.V. This is an open access article under the CC BY license (http://creativecommons.org/licenses/by/4.0/).

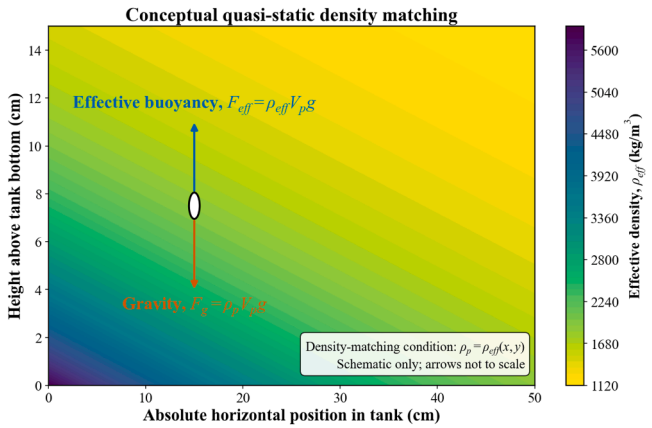



**Fig. 1.** Conceptual illustration of quasi-static density matching in magnetic density separation. Under the quasi-static approximation, a particle is predicted to approach a position where its density equals the local effective density of the magnetic liquid, $\rho_p = \rho_{eff(x,y)}$. The background colours represent the spatial effective-density field. The force arrows are schematic, are not drawn to scale, and do not represent a particle trajectory.

within a prescribed experimental domain, whereas constrained and multi-objective formulations incorporate admissibility requirements and trade-offs among indicators such as grade and recovery. Operating-window approaches further emphasize the value of identifying a robust region rather than only a single optimum [22]. Representative MDS studies have examined magnetic-liquid magnetization, particle size, initial particle distribution, flow disturbance, magnet configuration, and selected operating conditions [2,9,14,23]. However, a continuous, equipment-specific operating domain that combines ordered density-matching positions with minimum collection geometry has not yet been established for the present inclined-magnet MDS configuration.

Here, we construct an operating map from a quasi-static density-matching model using the measured magnetic-liquid density, $\rho_0(M_f)$, and established expressions for magnetic buoyancy and effective density [14,15]. Each ($\theta$, $M_f$) pair gives three bottom matching positions: the high/middle cut, a representative middle position, and the middle/low cut. The two cut positions, $x_h$ and $x_l$, delimit the three products, and $W_m = x_l - x_h$ is the width available for collecting the middle product. Feasibility is determined from position ordering, modeled field coverage, tank dimensions, particle size, and splitter thickness. The output is a feasible-domain and collection-window map for operating-condition screening. The calculated positions represent quasi-static equilibrium or deposition locations.

The primary objective of this study is to identify physically and geometrically feasible operating regions in the coupled $\theta - M_f$ space for MDS. The secondary objectives are to: (i) formulate a reproducible quasi-static effective-density and density-matching model incorporating experimental calibration; (ii) characterize the variability of the magnetic-liquid density calibration and assess the sensitivity of the predicted operating domain to the target cut densities, minimum collection-window criterion, particle size, and numerical grid resolution; (iii) document the practical implementation of the model-predicted splitter positions; and (iv) evaluate product partitioning at one representative operating condition through three independent separation experiments using product grade, mass yield, recovery, experimental variability, and mass- and elemental-balance closure. The experiments provide targeted evaluation of the selected condition rather than independent positional validation or complete experimental validation of the predicted domain.

## 2. Materials and methods

### 2.1. Materials, magnetic liquid, and separator configuration

The REE separation experiments used the 2–4 mm feed fraction. Before each run, the feed was homogenized and a representative portion was introduced into the separator by gravity without externally imposed bulk flow. The apparatus was checked for blockage, and the magnetic liquid was recirculated and ultrasonically dispersed to minimize nanoparticle agglomeration and boundary instability.

The operating-map calculations used a two-dimensional tank–magnet geometry with a tank length of 109.5 cm and a magnet length of 118.6 cm. Two 0.5 mm-thick splitters were placed at the predicted high/middle and middle/low cut positions, $x_h$ and $x_l$. The representative-condition plots display the upstream 0–50 cm region for clarity; this plotting limit does not alter the density-matching calculations or the reported cut positions. Other fixed apparatus and model inputs are summarized in Table 1. Here, $M_f$ (A/m) denotes the magnetization of the magnetic liquid, not magnetic-field intensity $H$.

A pilot-scale MDS apparatus developed by our group has previously been demonstrated for granular-waste sorting [14]. The present study, however, uses only the replicated laboratory-scale REE experiments for quantitative evaluation; the earlier pilot-scale demonstration is cited as apparatus background and is not used to validate the predicted operating domain.

The baseline magnetic-liquid density ($\rho_0$) was measured at $M_f$ = 0, 3368, 4000, 5250, and 12,000 A/m, giving mean densities of 1000, 1032, 1050, 1080, and 1250 kg/m$^3$, and corresponding standard deviations of 0, 18.1, 13.4, 8.9, and 21.9 kg/m$^3$, respectively. Piecewise-linear interpolation between adjacent calibration points was used in the model. Figure S1 shows the measurements and error bars. The global linear fit ($R^2 = 0.9659$; $RMSE = 16.20$ kg/m$^3$) describes only the overall calibration trend. The calibration measurements covered 0–12,000 A/m, whereas the operating maps were evaluated over 1000–12,000 A/m, within the calibrated range.

### 2.2. Quasi-static effective-density and density-matching model

A model related magnet angle $\theta$ and magnetic-liquid magnetization $M_f$ to the predicted collection positions. Let $x$ denote the absolute horizontal coordinate from the model origin and $y$ the height above the tank bottom. For an exponential magnetic-field decay with $k = \pi/L$, the effective density was calculated as

**Table 1**
Fixed model input and numerical settings.

| Parameter | Symbol | Value | Basis |
|---|---|---|---|
| Magnetic-field amplitude | $B_0$ | 0.63 T | Equipment specification |
| Characteristic pole length | $L$ | 0.19 m | Magnet geometry |
| Minimum magnet-to-tank distance | $d_{min}$ | 0.97 cm | Measured apparatus value |
| Maximum downstream extent of manual feed zone | $x_{feed,max}$ | 3.0 cm | Conservative observed feed-zone limit |
| Magnet angle range | $\theta$ | 5 – 15° | Investigated range |
| Magnetic-liquid magnetization range | $M_f$ | 1000–12,000 A/m | Operating-map range within calibration |
| Cut/representative densities | $\rho_h$, $\rho_m$, $\rho_l$ | 3300, 3100, 2900 kg/m$^3$ | Experimental density classes |
| Particle-size fraction | $d_p$ | 2–4 mm | Experimental feed |
| Splitter thickness | $t_s$ | 0.5 mm | Apparatus geometry |
| Minimum middle window | $W_{m^{min}}$ | 0.45 cm | Maximum particle diameter plus splitter thickness |
| Fine-grid resolution | $N_\theta \times N_{M_f}$ | 201 × 221 | $\Delta\theta = 0.05°$; $\Delta M_f = 50$ A/m |

$$\rho_{eff(x,y,\theta,M_f)} = \rho_0(M_f) + \left[\frac{\pi M_f B_0}{gL}\right]\exp\left\{-\frac{\pi[d_{min} + y + x\cdot\tan(\theta)]}{100L}\right\}, \quad (1)$$

where $g = 9.81\text{m/s}^2$; $x$, $y$, and $d_{min}$ are in centimetres; and division by 100 converts distance to metres. The derivation and nomenclature are provided in Supplementary Note S1.

Fig. 2 summarizes the calculation workflow and two-splitter product definition. The positions $x_h$ and $x_l$ define the two splitter locations, whereas $x_m$ is retained only as a representative middle-density position.

For a particle class of density $\rho_i$, the quasi-static matching locus satisfies $\rho_{eff(x,y,\theta,M_f)} = \rho_i$. At the tank bottom ($y = 0$), the corresponding absolute horizontal matching position is

$$x_i = \left\{-\left(\frac{100L}{\pi}\right)\ln\left[\frac{\Delta\rho_i gL}{\pi M_f B_0}\right] - d_{min}\right\}\Big/\tan(\theta). \quad (2)$$

Let $x_i$ denote the absolute horizontal coordinate of density-matching position $i$, measured from the model origin at the upstream inner wall of the tank. Unless otherwise stated, $x_h$, $x_m$, and $x_l$ use this same coordinate system. The particles were introduced manually within the upstream feed zone, $0 < x < x_{feed,\ max}$, for which a conservative downstream limit of $x_{feed,\ max} = 3.0$ cm was used in the feasibility check. The target densities $\rho_i = 3300$, 3100, and 2900 kg/m$^3$ define $x_h$, $x_m$, and $x_l$, respectively. Splitters placed at $x_h$ and $x_l$ define the high-grade ($0 < x < x_h$), middle-grade ($x_h < x < x_l$), and low-grade ($x > x_l$) regions. The middle-product collection-window width is

$$W_m = x_l - x_h. \quad (3)$$

Eq. (2) predicts equilibrium/deposition indicators rather than transient particle trajectories. The model assumes dilute particle loading, negligible particle–particle interactions, and sufficient time for particles to approach the density-matching regions. Lateral flow, particle inertia, transient drag, and residence-time distributions are not resolved. Particle transit time was not quantified because the opacity of the magnetic liquid prevented direct visual tracking; consequently, transient-trajectory and residence-time validation were outside the scope of this study.

Because the formulation is a quasi-static density-matching model rather than a transient transport model, viscosity, Reynolds number, drag coefficient, particle entry velocity, and residence time are not model inputs. Magnetic susceptibility is also not fitted independently because the experimentally controlled magnetic-liquid magnetization, $M_f$, is used directly in the effective-density expression.

### 2.3. Feasible operating domain and numerical assessment

Operating maps covered $5^\circ \leq \theta \leq 15^\circ$ and $1000 \leq M_f \leq 12000$ A/m. A condition was feasible only when all matching positions existed within the tank and magnetic-field coverage, retained the required ordering, and satisfied:

$$x_{feed,max} \leq x_h < x_m < x_l \leq x_{max},\ W_m \geq W_{m^{min}}. \quad (4)$$

Here, $x_{max}$ is the smaller of the tank length and the effective magnetic-field coverage. The first matching position was additionally required to lie downstream of the conservative feed-zone limit ($x_h > x_{feed,\ max} = 3.0$ cm). For the 2–4 mm feed fraction, the minimum middle-product collection width was defined as $W_{m^{min}} = 4.5$ mm (0.45 cm), equal to the upper particle-size limit (4.0 mm) plus the splitter thickness (0.5 mm). This provides geometric clearance for the largest particle and is an apparatus- and particle-size-specific criterion rather than a universal threshold.

The final operating map was evaluated on a 201 × 221 grid ($\Delta\theta = 0.05^\circ$; $\Delta M_f = 50$ A/m). Numerical convergence was assessed by comparison with medium and coarse grids using the maximum $W_m$, the feasible-domain fraction, and $W_m$ at $\theta = 12^\circ$ and $M_f = 5300$ A/m as convergence metrics (Figure S2 and Table S1). Sensitivity to the selected geometric criteria was evaluated by varying $W_{m^{min}}$ from 0.5 to 2.0 times its reference value and by applying particle-size-dependent criteria (Figures S3 and S4). The predicted matching positions and feasible-domain fraction were also evaluated after a simultaneous ±1% perturbation of the three target densities (Table S2). No utility penalty or empirically selected trade-off coefficient was used.

### 2.4. Experimental evaluation, sampling, and analytical quality control

A selected condition ($\theta = 12^\circ$ and $M_f = 5300$ A/m) was evaluated using three independent separation runs. At this condition, the model-predicted splitter positions were $x_h = 21.920$ cm and $x_l = 27.577$ cm. For the separation experiments, the splitter centre lines were manually set at 22.0 and 27.0 cm based on these model-predicted positions. The prescribed splitter positions defined the high-, middle-, and low-grade collection fractions, for which mass yield, TREO grade, and recovery were subsequently determined. Because the splitter positions were selected using the model rather than measured independently from particle streams or collection bands, the experiments evaluate product partitioning at the selected operating condition but do not provide

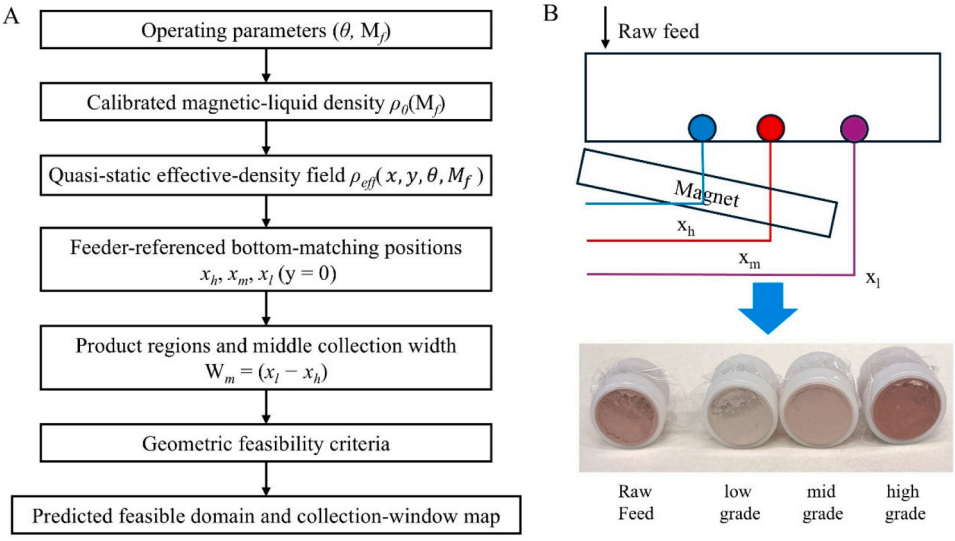



**Fig. 2.** Quasi-static density-matching workflow and two-splitter product definition. (A) Model calculation procedure. (B) Product regions defined by splitters at $x_h$ and $x_l$.

independent positional validation of the model. Each run produced high-, middle-, and low-grade fractions, which were collected and analysed separately. In each run, the feed and the high-, middle-, and low-grade products were collected and weighed separately. Product mass yield, mass-balance closure, elemental recovery, and elemental-balance closure were calculated as

$$Y_k = \left(\frac{m_k}{m_{feed}}\right) \times 100\%;\ c_{mass} = \left(\sum_k \frac{m_k}{m_{feed}}\right) \times 100\%, \tag{5}$$

$$R_k = \left(m_k c_k \,/\, m_{feed} c_{feed}\right) \times 100\%;\ c_{element} = \left(\sum_k \frac{m_k c_k}{m_{feed} c_{feed}}\right) \times 100\%, \tag{6}$$

where $m_k$ and $c_k$ are the mass and elemental concentration of product k, respectively, and $m_{feed}$ and $c_{feed}$ are the corresponding feed values. The feed and each product fraction from each separation run were analysed in triplicate by ICP. Triplicate ICP measurements were averaged for each sample. All performance indicators were then calculated separately for each separation run. The reported means and standard deviations therefore describe variability among the three independent runs (n = 3). Variability among the triplicate ICP measurements was reported separately as analytical repeatability.

For each run-level response, the 95% confidence interval of the mean was estimated via the Student's t-distribution as $\bar{x} \pm t_{0.975,n-1}\frac{s}{\sqrt{n}}$. With three independent separation runs (n = 3), $t_{0.975,2} = 4.303$ and the 95% confidence interval becomes $\bar{x} \pm 2.484$ s. The corresponding numerical 95% confidence intervals for grade, mass yield, recovery, mass-balance closure, and elemental-balance closure are reported in Table S3.

### 2.5. Analytical methods

After collection, each feed and product fraction was pulverized to <100 μm using a planetary ball mill (PM 100, Retsch, Germany) and homogenized before representative subsampling. Each analytical subsample was thoroughly mixed with a lithium borate flux and fused in a platinum crucible at >1000 °C to achieve complete decomposition of refractory rare-earth minerals. After cooling, the resulting glass bead was dissolved in dilute nitric acid. Rare-earth-element concentrations were determined by Inductively Coupled Plasma Mass Spectrometry (ICP-MS; iCAP TQ, Thermo Fisher Scientific, Germany) using the ME-MS81 method. Samples exceeding the applicable upper reporting limits were reanalysed using the ME-MS85h over-range method.

The stated duplicate and reference-material tolerances were 10% for ME-MS81 and 7% for ME-MS85h. These values were applied as batch quality-control acceptance criteria and were not interpreted as sample-specific measurement uncertainties. Analytical quality control included method blanks, laboratory duplicates, and the certified reference material AMIS0304. All reported quality-control results were within the applicable acceptance limits. Each feed and product sample was analysed in triplicate, with the within-sample standard deviation used to assess analytical repeatability.

## 3. Results and discussion

### 3.1. Predicted feasible domain and collection-window response

The calibrated quasi-static model converted each pair of magnet inclination angle ($\theta$) and magnetic-liquid magnetization ($M_f$) into three bottom density-matching positions. Application of the ordering, feed-zone, magnetic-field-coverage, tank-length, and minimum collection-width criteria produced the predicted feasible domain shown in Fig. 3A. White areas indicate parameter combinations that fail at least one geometric or ordering constraint. The feasible-domain fraction on the fine grid was 80.752%. The main outcome is therefore the identification of a broad feasible region rather than a single optimum.

Within the feasible domain, the middle-product collection width $W_m = x_l - x_h$ varied continuously with both operating variables (Fig. 3B). The maximum predicted $W_m$ was 14.225 cm over the evaluated grid. At the representative condition $\theta = 12^\circ$ and $M_f = 5300$ A/m, the predicted absolute cut positions were $x_h = 21.920$ cm and $x_l = 27.577$ cm, giving $W_m = 5.656$ cm. This provided ample clearance relative to the 0.45 cm minimum required for the 2–4 mm feed and 0.5 mm splitter thickness. The map identifies geometrically admissible conditions and shows how the available collection width changes across the operating domain. Final condition selection can then account for the required collection width and other practical operating considerations. The analysis assigns no utility-based ranking to these conditions.

The bounded feasible domain results from the existence, ordering, and spacing of the two predicted cut positions rather than from particle trajectories. At $\theta = 6^\circ$ and $M_f = 12{,}000$ A/m, $x_h$ was predicted at 95.905 cm, close to the usable magnetic-field limit ($x_{max}$), whereas $x_l$ was outside the usable region. At $\theta = 6^\circ$ and $M_f = 2500$ A/m, the maximum effective density within the accessible domain was 3285.03 kg/m$^3$, slightly below the 3300 kg/m$^3$ high/middle cut density; the corresponding analytical crossing was $x_h = -0.380$ cm, outside the upstream model boundary. Neither condition therefore provided the required ordered pair $x_h < x_l$ within the available collection region. Increasing $\theta$ shifted both cut positions upstream and reduced their separation; at $M_f = 5300$ A/m, $W_m$ decreased from 5.656 cm at $\theta = 12^\circ$

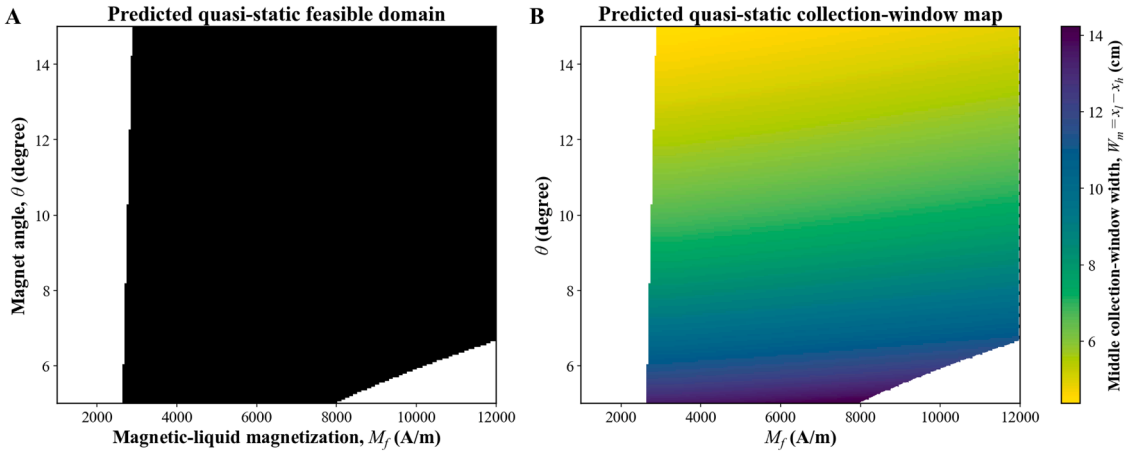



**Fig. 3.** Quasi-static operating maps. (A) Predicted feasible domain after application of the geometric and ordering constraints (black, feasible; white, infeasible). (B) Predicted middle-product collection-window width, $W_m = x_l - x_h$, within the feasible domain.

to 4.487 cm at $\theta = 15°$, although both conditions remained feasible under the 0.45 cm criterion. Thus, increasing either $M_f$ or $\theta$ does not necessarily improve the collection geometry, because feasibility depends on their coupled effects on the locations and separation of $x_h$ and $x_l$.

These trends follow from the quasi-static density-matching equations. Changing $\theta$ shifts the intersections of the density-matching loci with the tank bottom, whereas $M_f$ affects both the calibrated baseline liquid density and the magnetic contribution to the effective-density field. Feasibility therefore depends on their coupled effects and cannot be inferred from either variable alone. Increasing $M_f$ or $\theta$ did not monotonically improve the predicted collection geometry. Conditions were excluded when a required cut position lay outside the prescribed geometric limits or when $W_m$ fell below its minimum value. The map therefore supports constraint-based screening of operating conditions, with the final choice depending on the desired collection width and practical operating requirements.

### 3.2. Selected-input sensitivity and numerical convergence

Within the tested inputs and perturbation ranges, the operating-map predictions showed limited variation. Simultaneously perturbing the three target densities by ±1% changed $W_m$ at $\theta = 12°$ and $M_f = 5300$ A/m by <0.55% and changed the feasible-domain fraction by <0.19% relative to the baseline result (Table S2). Changing the minimum collection-window criterion shifted the feasible boundary because this threshold depends on particle size and separator geometry (Figure S3). Applying the particle-size-dependent criteria produced corresponding changes in the domain and normalized collection-window ratio (Figure S4). These results support preliminary use of the map within the stated input ranges and model assumptions; they do not demonstrate robustness to the apparatus parameters that were held fixed.

The grid-resolution analysis gave maximum $W_m$ values of 14.225 cm for the coarse, medium, and fine grids. At the selected condition, $W_m$ was 5.656 cm on all three grids. The feasible-domain fractions were 79.937%, 80.492%, and 80.752%, respectively; the medium–fine relative difference was 0.322%. The relative changes between the medium and fine grids were therefore below 0.33% for the selected convergence metrics, indicating that the 201 × 221 grid was sufficient for the operating-map calculations (Figure S2 and Table S1).

The five-point $\rho_0 - M_f$ calibration and its measured standard deviations provide the experimental basis for the magnetic-liquid baseline density. Piecewise-linear interpolation was used in the calculations, while the global linear fit ($R^2 = 0.9659$; $RMSE = 16.20$ kg/m$^3$) was retained only as a descriptive trend. The operating maps were restricted to 1000–12,000 A/m, within the measured calibration range. These choices avoid extrapolation but do not remove uncertainty between calibration points; denser calibration would be beneficial where the interpolation slope changes most strongly.

### 3.3. Experimental evaluation

Three independent runs were conducted at $\theta = 12°$ and $M_f = 5300$ A/m. Product performance was calculated separately for each run and is reported as the mean ± standard deviation across the three runs (n = 3). Triplicate ICP measurements were used only to assess analytical repeatability within each sample. Fig. 4 summarizes the experimental results at this condition. Figs. 4A and 4B show the inclined MDS apparatus and an example of the separated material, respectively, while Fig. 4C shows the location of the tested condition ($\theta = 12°$ and $M_f = 5300$ A/m) within the predicted collection-window map.

The high-, middle-, and low-grade products had mean TREO concentrations of 5.52, 1.75, and 1.17 wt%, respectively, compared with 2.31 wt% in the feed (Fig. 4D). The enrichment of the high-grade product and depletion of the low-grade product demonstrate density-based product partitioning at the tested condition. The corresponding grade, mass yield, recovery, mass-balance closure, and elemental-balance closure are summarized in Table S3 and are reported as mean

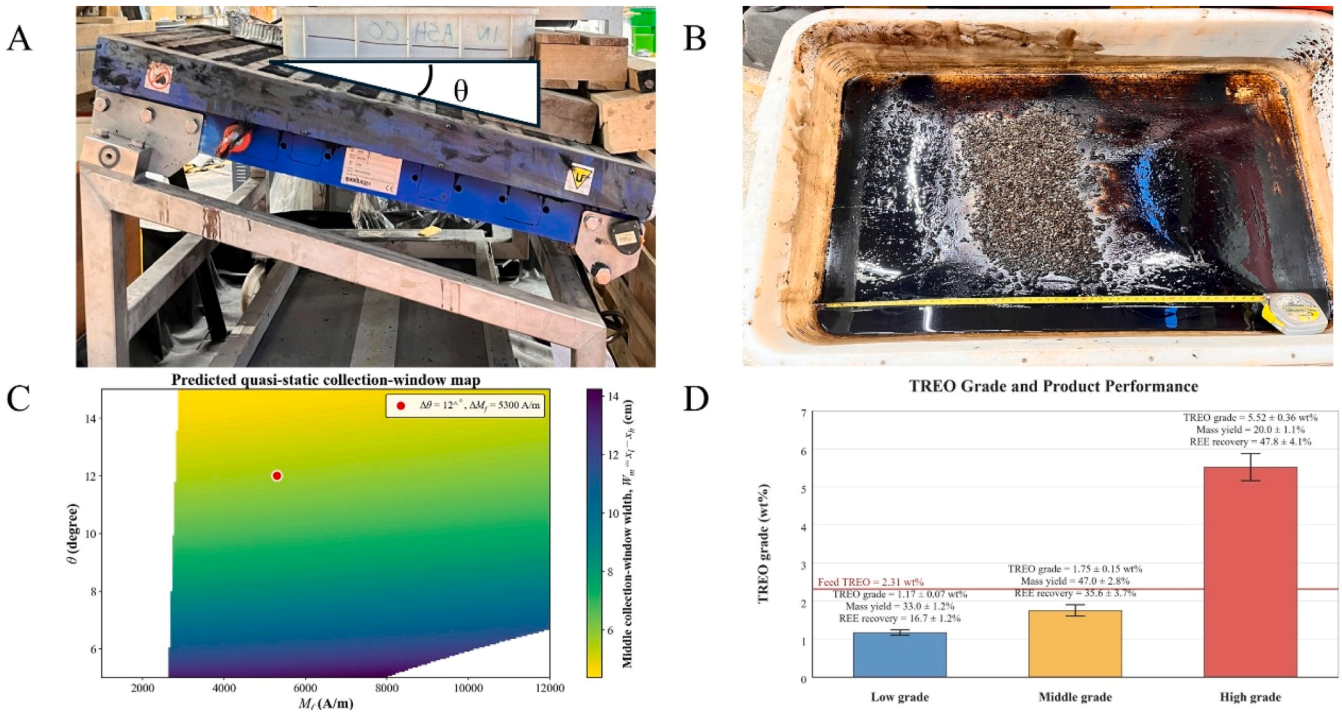



**Fig. 4.** Experimental evaluation of one representative operating condition. (A) Inclined MDS apparatus. (B) Example of separated material in the lab-scale tank. (C) Location of the representative condition ($\theta = 12°$, $M_f = 5300$ A/m) on the predicted collection-window map. (D) TREO concentrations, mass yields, and REE recoveries of the high-, middle-, and low-grade products obtained at this condition. Error bars represent the standard deviation across three independent separation runs (n = 3).

± standard deviation across the three independent separation runs.

Fig. 5 illustrates the physical interpretation of the predicted collection positions at the selected condition. Fig. 5A shows the effective-density field and the corresponding density-matching loci. At the tank bottom, the intersections of the effective-density profile with the high/middle and middle/low cut densities determine $x_h$ and $x_l$, respectively (Fig. 5B). These positions define the high-, middle-, and low-grade collection regions, while their separation, $W_m = x_l - x_h$, represents the available middle-product collection width. At $\theta = 12^\circ$, $M_f = 5300$ A/m, the predicted values were $x_h = 21.920$ cm and $x_l = 27.577$ cm, and $W_m = 5.656$ cm. Because the splitter positions were prescribed from the model-predicted $x_h$ and $x_l$ positions, the experimental results provide a targeted evaluation of product partitioning rather than independent positional validation. They do not validate the complete feasible domain.

No experimental conditions near or outside the predicted feasibility boundary were evaluated in the present study. Accordingly, the experiments assess product partitioning at the representative feasible condition but do not experimentally establish the location or shape of the complete feasibility boundary. Direct particle transit times could not be quantified because the opacity of the magnetic liquid prevented visual tracking. The observation that separation occurred rapidly was therefore not treated as a measured residence-time result. Transient particle trajectories, hydrodynamic effects, residence-time distributions, and process-energy consumption remain outside the scope of the present study.

### 3.4. Scope, limitations, and practical implications

The framework converts two coupled operating variables into an equipment-specific feasible domain. By making the constraints explicit, the map allows conditions to be selected according to practical considerations such as collection width, magnetic-liquid preparation, and apparatus requirements. For the present separator, it provides a practical basis for screening operating conditions and positioning the splitters.

The calculations describe quasi-static density-matching positions; transient particle motion, drag, residence time, and particle–particle interactions fall outside the model. The selected cut densities and the 0.45 cm collection-window criterion apply to the feed size and splitter geometry used here, while the five-point calibration limits the resolution of $\rho_0(M_f)$. Three independent separation runs were conducted at one tested condition, but conditions near or outside the predicted feasible-domain boundary were not tested. Energy performance was outside the scope of the study because neither comminution savings nor MDS energy consumption was measured.

Spatial magnetic-field mapping was not available to validate the assumed first-order field decay or the resulting two-dimensional effective-density field. It was used here to calculate the effective-density field for operating-condition screening. The sensitivity analysis examined calibration variability, target densities, collection-window criteria, particle-size-dependent criteria, and grid resolution. It did not vary the device parameters $B_0$, $L$, and $d_{min}$, for which experimentally supported ranges or uncertainty distributions were unavailable. The sensitivity results should therefore be interpreted within the input ranges examined here. The 3.0 cm feed-zone boundary was based conservatively on the observed manual feeding procedure.

Experimental testing near the predicted boundary is now the most important validation step. Spatial magnetic-field measurements, additional $\rho_0 - M_f$ calibration points, controlled feed-position measurements, and tracer experiments in an optically accessible system would provide stronger tests of the model assumptions and the predicted operating-domain boundaries.

## 4. Conclusions

This study developed a constraint-aware operating-map approach for determining feasible conditions in MDS by considering the coupled effects of magnet inclination angle $\theta$ and magnetic-liquid magnetization $M_f$. Instead of maximizing $M_f$ or selecting a single mathematical optimum, the framework identifies combinations of $\theta$ and $M_f$ that satisfy the required ordering of density-matching positions, magnetic-field coverage, tank geometry, and minimum collection width. The resulting map shows that suitable separation conditions occur within a bounded operating region and that the available middle-product collection width varies substantially across this region. At $\theta = 12^\circ$ and $M_f = 5300$ A/m, the predicted $x_h$, $x_l$, and $W_m$ were 21.920, 27.577, and 5.656 cm, respectively. The predicted domain showed limited variation under the tested cut-density perturbations and grid refinements. Three independent runs at the selected condition demonstrated density-based product partitioning among the collected products. Validation across a wider range of operating conditions remains necessary. Overall, the proposed framework shifts MDS operation from individual-parameter maximization towards the identification of practically collectable operating regions and provides a transparent basis for operating-condition selection and splitter placement.

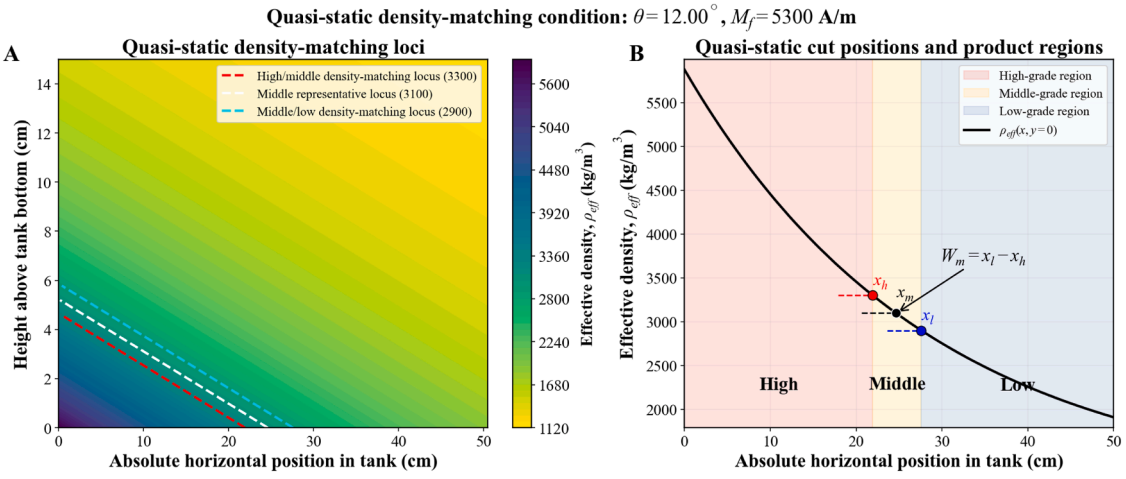



**Fig. 5.** Representative quasi-static density-matching prediction at $\theta = 12^\circ$ and $M_f = 5300$ A/m. (A) Effective-density field and density-matching loci for the three target densities. (B) Bottom effective-density profile, predicted cut positions, and corresponding product regions.

## CRediT authorship contribution statement

**Hongli Su:** Writing – original draft, Visualization, Validation, Software, Methodology, Investigation, Formal analysis, Data curation, Conceptualization. **Kunning Tang:** Writing – original draft, Software, Formal analysis. **Max van Beek:** Investigation, Formal analysis, Data curation. **Peter Rem:** Writing – review & editing. **Zhenkai Bo:** Writing – original draft, Software, Formal analysis. **Rajeev Bheemireddy:** Formal analysis, Data curation. **Nishab Ali:** Writing – review & editing. **Yongli Wu:** Writing – review & editing, Supervision. **Francesco Di Maio:** Writing – review & editing, Supervision, Resources, Funding acquisition.

## Declaration of competing interest

The authors declare that they have no known competing financial interests or personal relationships that could have appeared to influence the work reported in this paper.

## Acknowledgements

This work has received funding from the European Union's Horizon 2020 and Horizon Europe research and innovation programmes under Grant Agreements No. 958302 and No. 101138353. The APC was funded by the TU Delft Library. The authors also gratefully acknowledge Myne Circular Metals, the Netherlands, for its technical support.

## Supplementary materials

Supplementary material associated with this article can be found, in the online version, at doi:10.1016/j.rineng.2026.113344.

## Data availability

Data will be made available on request.

## References

[1] R.L. Smith, S. Behdad, From present to future: a review of e-waste recycling processes, Waste Manage. 204 (2025) 114863.
[2] S. Tajfirooz, et al., Direct numerical simulation of magneto-archimedes separation of spherical particles, J. Fluid. Mech. 910 (2021) A52.
[3] B. Hu, Magnetic density separation of polyolefin wastes, Open Waste Manage. J. (2014).
[4] N.A.H.B. Awang Kechik, K.E.H. Ku Ishak, Optimizing monazite recovery from tin tailings: a comprehensive review of physical techniques and methodologies, Physicochemic. Problem. Mineral Process. 61 (6) (2025) 215442.
[5] J. Svoboda, Densimetric separation of coal using magnetic fluids, Physic. Separat. Sci. Eng. 13 (3–4) (2004) 127–139.
[6] van Beek, M., *The golden age of wasted TVs*. 2022.
[7] A.J. Whitworth, et al., Review on advances in mineral processing technologies suitable for critical metal recovery from mining and processing wastes, Cleaner Eng. Technol. 7 (2022) 100451.
[8] P.C. Rem, S.P.M. Berkhout, Magnetic Density Separation Device and Method, Google Patents, 2021.
[9] L. Thijs, et al., Magnetic density separation of particles in honeycomb-generated wake turbulence, Chem. Eng. Sci. 278 (2023) 118930.
[10] V. Luciani, et al., Upgrading of PVC rich wastes by magnetic density separation and hyperspectral imaging quality control, Waste Manage. 45 (2015) 118–125.
[11] G. Ballantyne, M. Powell, Benchmarking comminution energy consumption for the processing of copper and gold ores, Miner. Eng. 65 (2014) 109–114.
[12] D. Tromans, Mineral comminution: energy efficiency considerations, Miner. Eng. 21 (8) (2008) 613–620.
[13] D. Fuerstenau, A.-Z. Abouzeid, The energy efficiency of ball milling in comminution, Int. J. Mineral Process. 67 (1–4) (2002) 161–185.
[14] L. Wang, et al., An innovative magnetic density separation process for sorting granular solid wastes, Recycling 9 (3) (2024) 48.
[15] J. Svoboda, Magnetic Techniques For the Treatment of Materials, Springer, 2004.
[16] J. Kosse, et al., Thermal and electrical design of superconducting demonstrator for magnetic density separation, Superconductor Sci. Technol. 35 (6) (2022) 064002.
[17] J. Kosse, et al., Mechanical design of a superconducting demonstrator for magnetic density separation, Superconduct. Sci. Technol. 34 (11) (2021) 115019.
[18] J. Kosse, et al., Optimum coil-system layout for magnet-driven superconducting magnetic density separation, IEEE Trans. Magn. 57 (8) (2021) 1–9.
[19] N. Aslan, Modeling and optimization of Multi-Gravity Separator to produce celestite concentrate, Powder Technol. 174 (3) (2007) 127–133.
[20] N. Aslan, Multi-objective optimization of some process parameters of a multi-gravity separator for chromite concentration, Sep. Purif. Technol. 64 (2) (2008) 237–241.
[21] C. Guria, et al., Simultaneous optimization of the performance of flotation circuits and their simplification using the jumping gene adaptations of genetic algorithm-II: more complex problems, Int. J. Mineral Process. 79 (3) (2006) 149–166.
[22] D.P. Clausing, Operating window: an engineering measure for robustness, Technometrics 46 (1) (2004) 25–29.
[23] B. Hu, et al., Magnetization control of magnetic liquids for sink-float separations, Open Waste Manage. J. 3 (2010) 81–89.